

Accepted Manuscript

Compositional data analysis of Holocene sediments from the West Bengal Sundarbans, India: Geochemical proxies for grain-size variability in a delta environment

R.P. Flood, M.R. Bloemsma, G.J. Weltje, I.D. Barr, S.M. O'Rourke, J.N. Turner, J.D. Orford

PII: S0883-2927(16)30114-7

DOI: [10.1016/j.apgeochem.2016.06.006](https://doi.org/10.1016/j.apgeochem.2016.06.006)

Reference: AG 3673

To appear in: *Applied Geochemistry*

Received Date: 5 November 2015

Revised Date: 13 June 2016

Accepted Date: 22 June 2016

Please cite this article as: Flood, R.P., Bloemsma, M.R., Weltje, G.J., Barr, I.D., O'Rourke, S.M., Turner, J.N., Orford, J.D., Compositional data analysis of Holocene sediments from the West Bengal Sundarbans, India: Geochemical proxies for grain-size variability in a delta environment, *Applied Geochemistry* (2016), doi: [10.1016/j.apgeochem.2016.06.006](https://doi.org/10.1016/j.apgeochem.2016.06.006).

This is a PDF file of an unedited manuscript that has been accepted for publication. As a service to our customers we are providing this early version of the manuscript. The manuscript will undergo copyediting, typesetting, and review of the resulting proof before it is published in its final form. Please note that during the production process errors may be discovered which could affect the content, and all legal disclaimers that apply to the journal pertain.



1 **Compositional data analysis of Holocene sediments from the West Bengal**
2 **Sundarbans, India: geochemical proxies for grain-size variability in a delta**
3 **environment**

4

5 R.P. Flood^{1,2*}, M.R. Bloemsa³, G.J. Weltje⁴, I.D. Barr¹, S.M. O'Rourke⁵, J.N. Turner⁶,
6 J.D. Orford¹

7 ¹School of Geography, Archaeology, and Palaeoecology, Queen's University Belfast,
8 BT7 1NN, Northern Ireland, UK

9 ²Present address: School of Natural Sciences, Trinity College Dublin, Dublin 2, Republic
10 of Ireland

11 ³Tata Steel - Netherlands Main Office, Postbus 10000, 1970 CA IJmuiden, The
12 Netherlands

13 ⁴Department of Earth and Environmental Sciences, Geology Division, University of
14 Leuven, Celestijnenlaan 200E, 3001 Leuven-Heverlee, Belgium

15 ⁵School of Biosystems Engineering, University College Dublin, Belfield, Dublin 4,
16 Republic of Ireland

17 ⁶School of Geography & UCD Earth Institute, University College Dublin, Belfield,
18 Dublin 4, Republic of Ireland

19

20 * Corresponding author. Email Address: rpfflood@tcd.ie Phone number: +35318962661

21

22 Keywords: compositional data; Ganges-Brahmaputra delta; XRF; calibration;
23 geochemistry; grain-size; partial least squares.

24 **ABSTRACT**

25 This paper is part of a special issue of Applied Geochemistry focusing on reliable
26 applications of compositional multivariate statistical methods. This study outlines the
27 application of compositional data analysis (CoDa) to calibration of geochemical data and
28 multivariate statistical modelling of geochemistry and grain-size data from a set of
29 Holocene sedimentary cores from the Ganges-Brahmaputra (G-B) delta. Over the last two
30 decades, understanding near-continuous records of sedimentary sequences has required
31 the use of core-scanning X-ray fluorescence (XRF) spectrometry, for both terrestrial and
32 marine sedimentary sequences. Initial XRF data are generally unusable in ‘raw-format’,
33 requiring data processing in order to remove instrument bias, as well as informed
34 sequence interpretation. The applicability of these conventional calibration equations to
35 core-scanning XRF data are further limited by the constraints posed by unknown
36 measurement geometry and specimen homogeneity, as well as matrix effects. Log-ratio
37 based calibration schemes have been developed and applied to clastic sedimentary
38 sequences focusing mainly on energy dispersive-XRF (ED-XRF) core-scanning. This
39 study has applied high resolution core-scanning XRF to Holocene sedimentary sequences
40 from the tidal-dominated Indian Sundarbans, (Ganges-Brahmaputra delta plain). The
41 Log-Ratio Calibration Equation (LRCE) was applied to a sub-set of core-scan and
42 conventional ED-XRF data to quantify elemental composition. This provides a robust
43 calibration scheme using reduced major axis regression of log-ratio transformed
44 geochemical data. Through partial least squares (PLS) modelling of geochemical and
45 grain-size data, it is possible to derive robust proxy information for the Sundarbans
46 depositional environment. The application of these techniques to Holocene sedimentary

47 data offers an improved methodological framework for unravelling Holocene
48 sedimentation patterns.

49

50 **1. GEOCHEMISTRY OF HOLOCENE SEDIMENTARY ENVIRONMENTS**

51 The composition and physical properties of sediments and sedimentary rocks are for the
52 most part controlled by chemical processes taking place during weathering, transport, and
53 burial (diagenesis) (Bjørlykke, 2010). Thus, understanding the physical properties of
54 sediments and sedimentary rocks requires an understanding of the chemical processes
55 underlying sedimentary deposition. The formation of clastic sediments is a result of the
56 erosion and weathering of source parent rocks. The dissolved fraction of this clastic
57 sediment flows into seas or lakes, with subsequent precipitation as biological or chemical
58 sediments. During transport, grains continue to undergo weathering and abrasion, with
59 resultant sediments potentially undergoing repeated cycles of deposition and erosion prior
60 to final deposition. In order to establish the origin of these sediments, and to gain an
61 understanding of the processes that have operated prior to their deposition, there is a need
62 to analyse their geochemistry. For Holocene sediments (i.e., those deposited within the
63 last 11.7 ka), environmental geochemistry offers a series of approaches to analyse
64 sediment geochemistry. For example, the identification of minerals in soils and sediments
65 usually involves high powered electron microscopy to image crystal forms, and
66 diffraction and vibrational spectroscopy to determine crystallographic structures (Ryan,
67 2014). Understanding the elemental composition of sediment usually involves the
68 analysis of elemental absorbance, emission, fluorescence or mass (Ryan, 2014). These
69 approaches to elemental analysis fall into two groups: destructive and non-destructive.

70 The former involve the dissolution of minerals into an aqueous solution, whilst the latter
71 are characterised by the analysis of mineral powders (Ryan, 2014). These non-destructive
72 approaches include X-ray fluorescence (XRF) which this study will examine for the
73 purposes of the chemometric calibration of element geochemistry from the Sundarbans,
74 West Bengal, India. This paper provides a background to XRF, XRF core-scanning and
75 calibration through compositional data analysis (CoDa), with a focus on the sediments of
76 the Sundarbans, to demonstrate the usefulness of the techniques. Through the application
77 of CoDa, a number of calibration coefficients can be derived for key proxy geochemical
78 indicators and used to study sedimentary provenance and depositional processes. The
79 objective of the study is to investigate how the application of LRCE & PLS to Holocene
80 sediments of a Delta environment can improve interpretation of geochemical indicators
81 of grain-size variability.

82

83 **2. BACKGROUND TO THE INDIAN SUNDARBANS**

84 The Sundarbans is one of the largest coastal wetland sites in the world (~ 1 million
85 hectares) covering the western delta of the Ganges and Brahmaputra (G-B) rivers (Fig.
86 1). The Sundarbans is a complex network of tidal creeks and deltaic islands with most
87 sediment arriving indirectly from the G-B river systems (which drain the Himalayas).
88 The Indian Sundarbans comprises just over 400,000 hectares in the western sector of the
89 G-B delta, and is cross-cut by a number of approximately north-south estuarine channels
90 (Fig. 2). Overall, the G-B delta is generally divided into two sub-systems of fluvially and
91 non-fluvially dominated depositional environments (Fig. 1) (Rogers et al., 2013). The
92 eastern sector of G-B delta comprises the fluvially dominated system, whilst the older

93 abandoned part of the delta, in the west, comprises the non-fluvially dominated
94 environment that is no longer directly linked to the G-B river sources (Fig. 1). This
95 western part of the delta (which underlies the present day Indian Sundarbans) was
96 fluvially abandoned prior to c. 5000 cal yr BP, as the Ganges River migrated eastward
97 towards its present position (Goodbred and Kuehl, 2000). Shoreline progradation in the
98 eastern delta complex following the joining of the Ganges and Brahmaputra rivers in the
99 Meghna Estuary is considered to be fluvially-dominated (Allison, 1998a).

100 The western extent of the G-B delta is now thought to be undergoing net delta
101 front erosion (Allison, 1998b; Allison et al., 2003), likely reflecting an eroding
102 environment in areas distal to areas of contemporary fluvial-deltaic deposition (Allison
103 (1998b). As the Ganges river shifted from its former western discharge channel (i.e.,
104 Hoogly River) to its current position in the east, a series of palaeo-distributary channels
105 were left abandoned (Allison, 1998b). These channels reflect an almost exclusively tidal-
106 driven geomorphology, with sediments and discharge from the main G-B rivers no longer
107 entering the western delta front (Allison, 1998b; Bhattacharyya et al., 2013).

108 In order to fully explore the processes of sedimentation and the potential sources
109 of variance in sediment composition during the late-Holocene (post Ganges shift), high
110 resolution data analysis is required. Such analysis has never been performed on
111 sedimentary cores from the Sundarbans, and this study represents the first attempt at
112 characterising the sedimentary facies using high-resolution core-scan XRF and
113 establishing variation in sediment deposition.

114

115 **3. INTRODUCTION TO XRF CORE-SCANNING**

116 The application of X-ray fluorescence (XRF) to geological materials is well established,
117 and recognised as a conventional technique for deriving elemental composition (Ramsey
118 et al., 1995; Jenkins, 1999; De Vries and Vrebos, 2002; Weltje and Tjallingii, 2008). The
119 underlying principle of XRF analysis is that excitation of electrons by incident X-
120 radiation (X-rays) leads to the ejection of electrons from the inner ring of an atomic shell.
121 This ejection results in a vacancy, which is filled by cascading electrons from the outer
122 shells, which, in turn, leads to the emission of energy (Weltje and Tjallingii, 2008). The
123 emitted energy and wavelength spectra are atomically indicative of particular elements,
124 allowing relative abundances of elemental compositions to be derived (Weltje and
125 Tjallingii, 2008).

126 In the 1990s, the development of a non-destructive core logging technique which
127 applies XRF for the determination of major-element concentrations in split sediment
128 cores was first utilised by the Royal Netherlands Institute for Sea Research (NIOZ)
129 (Jansen et al., 1998). The most advantageous surface for XRF sample determination is
130 homogeneous, dry, and smooth (Jansen et al., 1998). Using split-cores surfaces provides
131 comparable geochemical data to powder samples (Jansen et al., 1998). This is due to the
132 response depths that vary between elements. However, it has been found problematic that
133 larger particles tend to attenuate the fluorescent radiation of elements more than fine
134 particles (Jansen et al., 1998). The 'ideal' homogeneity of a sample occurs when the
135 majority of the material can pass through a 70-mm sieve (Potts, 1987; Jansen et al.,
136 1998), with 'ideal' results derived from silts and clays, rather than from sands (which
137 require careful interpretation of results) (Jansen et al., 1998). The key advantages of XRF
138 core-scanning over conventional geochemical analysis of discrete specimens is that

139 element intensities are obtained directly at the surface of a split sediment core (allowing
140 for the extraction of near-continuous records of element intensities), and the spatial
141 resolution of ED-XRF core-scanning is much higher than conventional discrete sampling
142 destructive methods (Weltje and Tjallingii, 2008). However, one of the main drawbacks
143 of the approach has been the conversion of element intensities measured by ED-XRF
144 core-scanners to element concentrations (Weltje and Tjallingii, 2008). Thus, the results
145 obtained by ED-XRF core-scanning are generally presented in the form of count rates
146 (counts per unit time per unit area), or as ratios of counts, count rates, or intensities of
147 elements (Richter et al., 2006; Rothwell et al., 2006; Thomson et al., 2006; Weltje and
148 Tjallingii, 2008). Within regular calibration schemes, measurement geometry and
149 specimen homogeneity is very poorly constrained due to the inhomogeneity of samples
150 and the irregular surface of a split-core (Weltje and Tjallingii, 2008; Weltje et al., 2015).
151 In addition, in some instances, spatial variations in the thickness of an adhesive pore-
152 water film which forms directly below a protective polyester film covering the split core
153 surface should be considered a further constraining factor on measurement geometry
154 values in the calibration equation (Weltje and Tjallingii, 2008). Due to these poorly
155 constrained and uncontrollable variations in the experimental setup, the measurement
156 geometry becomes an 'unknown' in the calibration equation and renders its solution
157 intractable within reasonable limits of uncertainty (Weltje and Tjallingii, 2008). As a
158 result of this uncontrollable variable in the calibration equation, the experimental setup of
159 quantitative XRF core-scanning must incorporate control specimens of known intensities
160 (Weltje and Tjallingii, 2008). However, such calibration approaches often possess
161 inherent intractability which can make the exercise inappropriate for fully quantifying

162 core-scan ED-XRF intensities. As a result, calibration requires an alternative approach
163 within the scope of CoDa in the form of the Log-Ratio Calibration Equation (LRCE): a
164 univariate log-ratio calibration (ULC) approach that combines conventional calibration
165 approaches in ratio form (Weltje et al., 2015).

166 The primary justification for the application of the LRCE and calibration in this
167 study is outlined by Bloemsma (2015) in terms of deriving meaningful data. Essentially,
168 the reason why calibration of core-scan derived XRF data is that if calibration is not
169 performed, no actual useful information other than noise and ‘presence/absence’ of
170 particular elemental data can be discerned. Calibrating the data in the manner outlined in
171 this manuscript actually shows robustly both the relative elemental composition present,
172 but also that the elements that are calibrated are actual signal as opposed to noise.

173

174 **4. METHODOLOGY**

175 4.1. Quantification of core-scan derived XRF through the LRCE

176 The LRCE works by using the relationship between elements derived from core-scan and
177 conventional ED-XRF. Core-scan ED-XRF cannot be calibrated in standard equations
178 due to unknown coefficients of such models, as it is not possible to correct for grain-size,
179 water content etc., on a split core log without altering the sample. In principle, calibration
180 of conventional ED-XRF faces the problems of being a closed dataset (i.e., appropriate
181 data for compositional data analysis), but still representative of relative quantities of
182 elements in a sample. However, although core-scan ED-XRF is semi-quantitative (i.e.,
183 data are in form of counts per second) there are also relative abundances of elements (i.e.,
184 core-scan ED-XRF counts are relative to the sum-total of counts that are present between

185 each element). If a series of points is measured using core-scan ED-XRF and
186 subsequently sub-sampled and processed with conventional ED-XRF, then there are two
187 datasets for the same sample: conventional ED-XRF and core-scan ED-XRF.

188 The two datasets that are modelled in the LRCE are the core-scan ED-XRF counts
189 (i.e., intensity data) for which the concentration is unknown, and the concentration values
190 (e.g., %, ppm, etc.) dataset from the same set of samples as the intensity data, that form
191 the reference dataset in the calibration procedure. The way in which the LRCE works is
192 that the empirical model coefficients α and β are the log-ratio equivalents of the matrix
193 effect and detection efficiency (this is true in the case of single-element XRF
194 spectrometry), respectively (Weltje and Tjallingii, 2008). The LRCE uses a number of
195 independent models for the binary sub-compositions of a given set of elements to the
196 spectrum of relative XRF intensity data by using major axis regression based on singular
197 value decomposition (SVD) (Weltje and Tjallingii, 2008).

198 The LRCE can be considered a form of additive log-ratio transformation (alr)
199 (Aitchison, 1982; 1986), whereby the transformation is performed on every linear
200 combination of the sub-compositions examined (Weltje and Tjallingii, 2008). The key
201 principle however is that the calibration functions in log-ratio space and that these are
202 linear. After which, inverse log-ratio transformation and closure, the same data can be
203 expressed in relative intensities against concentrations in binary composition (Weltje and
204 Tjallingii, 2008). Predictions of the most optimum log-ratio denominator are allowed for
205 in this approach which reduces any non-linearity introduced by matrix effects (Weltje and
206 Tjallingii, 2008). Although the calibration process is carried out in log-ratio space it is
207 possible to inverse-transform the results using the inverse-alr function, giving

208 compositional data as output (Weltje and Tjallingii, 2008; Bloemsma, 2010). The LRCE
209 derives multiple element composition estimates from XRF core-scanner output by fitting
210 a series of mutually independent models for binary sub-compositions of elements to the
211 spectrum of (relative) intensities (Weltje and Tjallingii, 2008). The variables are only
212 considered in the form of dimensionless log-ratios, which implies that normalisation prior
213 to analysis is not relevant, and this is consistent with the key tenets of the CoDa approach
214 (Weltje and Tjallingii, 2008). With this in mind, the model is unconstrained from the
215 unit-sum and non-negativity problems imposed by a closed dataset (Weltje and Tjallingii,
216 2008). A full derivation of the LRCE is given in Weltje and Tjallingii (2008) and Weltje
217 et al. (2015).

218 In this study the prediction of the ED-XRF core-scan sub-composition was carried out
219 according to the following scheme:

- 220 • The core-scan intensity ED-XRF data and the percentage (%) concentration
221 PXRF data are examined for the α and β model parameters through major axis
222 regression by SVD (Press et al., 1994).
- 223 • Binary sub-compositions between intensity ED-XRF (core-scan) and %
224 concentration PXRF are plotted (i.e., the optimum log-ratio denominator that
225 gives the best linear fit is derived and a series of alr-transformations are used
226 employing this optimum log-ratio denominator, to derive a linear relationship
227 between % concentration data and intensity data).
- 228 • The best fit model for intensity ED-XRF – the ED-XRF data from both the %
229 concentration and predicted concentration are permuted and calculated for each
230 log-ratio pair of linear distances, which derives the best fit for the intensity ED-

- 231 XRF sub-composition (Weltje and Tjallingii, 2008). This is empirically quantified
232 by taking the median of the squared discrepancies between the predicted and the
233 % concentration geochemical composition with discrepancies calculated through
234 the use of a 'leave-one-out-cross-validation' (LOOCV) (Bloemsma et al., 2012).
- 235 • The Aitchison distance between predicted and reference composition is used as
236 the determinant for the optimal denominator element in the sub-composition (i.e.,
237 the residual variance between measurements in both the regression and predicted
238 models) (Bloemsma et al., 2012).
 - 239 • The goodness-of-fit of the optimum log-ratio denominator is derived from the
240 residual variance and the total variance (Weltje and Tjallingii, 2008).
 - 241 • The relative abundance of each element in the sub-composition from the predicted
242 weights is determined through an inverse alr-transformation, with data expressed
243 in a conventional (closed) form (Weltje and Tjallingii, 2008).

244 Data from core-scan derived ED-XRF are now calculated based on the relative
245 abundances of the sub-composition. However, to perform any further statistical analysis
246 of the data, they are required to be subjected to further log-ratio transformation (e.g., alr-,
247 centred log-ratio (clr), or isometric log-ratio (ilr) transformation). As the LRCE is
248 founded on the CoDa principles, the use of a common log-ratio denominator is
249 unrestricted and functions as a normalisation approach (Weltje and Tjallingii, 2008). The
250 use of a common log-ratio denominator in the calibration model is generally independent
251 of any environmental or sedimentological considerations (i.e., the log-ratio denominator
252 is independent of any physical reasoning for use in the calibration model) (Weltje and
253 Tjallingii, 2008).

254 4.3 Joint geochemical and grain-size modelling

255 Grain-size and geochemical composition of clastic sediments have been found to be
256 highly correlated as a result of the processes that control the generation of sediment from
257 crystalline rocks (Bloemsma et al., 2012). The composition of modern sediments and
258 their grain-size variation is due to four key factors: (i) contributions of mineralogically
259 and texturally distinct grains from a number of divergent sources (ii) rock fragments
260 being mechanically weathered into a finer composition, (iii) labile grains being more
261 susceptible to chemical weathering and (iv) transport associated sorting of
262 compositionally distinct grains (Whitmore et al., 2004).

263 Bloemsma et al. (2012) have expanded on this relationship between geochemical
264 and modal grain-size variation, as geochemical variation is generally considered to reflect
265 the pervading environmental conditions of sediment genesis. In terms of relating grain-
266 size variation to bulk geochemical composition, it may be postulated in terms of the
267 chemical weathering of crystalline rocks, in which the release of unstable elements as
268 solutes takes place, whereas elements such as Al remain in the solid phase (Nesbitt and
269 Young, 1984; Bloemsma et al., 2012).

270 The development of the PLS modelling approach for joint geochemical and grain-
271 size relationships is premised on whether in a series of sediment samples derived from a
272 source area that, over time the extent of chemical weathering was static, then the bulk
273 geochemical variation may be attributed to; selective entrainment, transport, and
274 deposition (Bloemsma et al., 2012). In a sedimentological context, such a one-to-one
275 relationship between grain-size and geochemistry is rare with geochemical variability
276 being a function of: chemical weathering; hydraulic/aerodynamic sorting; mixing; and

277 diagenesis (Bloemsma et al., 2012). In these regards, the variability between grain-size
278 and geochemistry is considered as being what is shared and what is unshared, in which
279 case if the former is removed from the data and the residuals calculated, then unknown
280 trends such as provenance may be distinguished as a result (Bloemsma et al., 2012).

281 The partial least squares (PLS) modelling approach was developed by Bloemsma
282 et al. (2012) and has two key assumptions: (1) that there is a monotonic relationship
283 between grain-size and geochemical composition, and; (2) grain-size distributions and
284 geochemical compositions are both compositional in nature, necessitating the use of
285 models in log-ratio space (Bloemsma et al., 2012).

286 Effectively, geochemical data are considered to contain two parts, with one part
287 that is correlated with grain-size, and a second part which varies independently from
288 grain-size (Bloemsma et al., 2012). The model is carried out by finding a basis for which
289 maximizes the geochemical variance explained by the grain-size (Bloemsma et al., 2012).
290 If then, the mean is subtracted from these geochemical and grain-size data matrices, the
291 values of the residuals are provided (Bloemsma et al., 2012). If there is significantly high
292 correlation found in the projection of both datasets onto the basis vectors, then these are
293 considered to be the 'shared signals' (Bloemsma et al., 2012). The residual signal is then
294 calculated by subtraction of the shared signals from the raw data, giving the variability
295 unique to each dataset (Bloemsma et al., 2012). Taking Fig. 3 for example where $X \setminus Y$
296 could be considered to represent grain-size variability and $Y \setminus X$ representative of
297 geochemical variability, the variability shared by both data sets is indicated by $X \cap Y$,
298 which is highlighted in grey (Bloemsma et al., 2012). In contrast to this shared
299 variability, the variability that is then unique to the geochemical data that potentially

300 holds relevant signals (e.g., provenance) is shown by $Y \setminus X$, representing the residual
301 geochemical variability (Bloemsma et al., 2012).

302 The implementation of the PLS modelling approach follows on from the work of
303 Bloemsma et al. (2012) in which:

- 304 • clr-transformation of both the grain-size and geochemical data.
- 305 • Derive the basis Q (i.e., clr-transformed geochemical solution space) in \mathbb{R}^D that
306 can maximise the geochemical variance explained by the grain size through the
307 Partial Least Squares (PLS) (Wold et al., 1982).
- 308 • Fit a model onto data matrices X^* (where $X = L$ grain size classes) and Y^* (where
309 $Y = D$ variables).
- 310 • Subtract the mean from the X^* and Y^* to derive X_c^* and Y_c^* through the SIMPLS
311 algorithm (de Jong, 1993) and calculate the PLS matrix decomposition.
- 312 • Orthogonalise the bases (i.e., the loadings) through SVD with the score matrices
313 recalculated.
- 314 • Test the significance of correlation between geochemistry and grain-size
315 distribution scores on the k -th basis vector using the Kendall and Stuart (1973)
316 test.
- 317 • Derive r for any order of k , where r is the Pearson's correlation coefficient
318 between the k -th column and the previously orthogonalised bases.
- 319 • With a confidence level of α and $p = 1 - \alpha$, the first k of shared signals is removed
320 if for the k the Kendall and Stuart (1973) criterion is established.

- 321 • The model is applied to all grain-size and geochemical data as the transpose of the
322 bases are orthonormal, thus the scores of all observed grain-size distributions and
323 geochemical compositions may then be derived by the matrix product.
- 324 • Reduced-rank approximation is used to derive the shared signal in both the grain-
325 size and geochemistry datasets.
- 326 • Residuals calculated and subtracted from the common variability for both the
327 GSDs and geochemistry input data.
- 328 • Mean added, such that the residual signals centre around the mean of their
329 corresponding raw data matrix (Bloemsma et al., 2012).

330 Through this algorithm implementation it may be possible to derive the grain-size
331 dependent and independent geochemical components from the dataset. The reader is
332 referred to Bloemsma (2010), Bloemsma et al. (2012), and Bloemsma (2015)
333 publications for a more exhaustive discussion on the PLS algorithm. However, it is only
334 through utilising the calibrated geochemical data presented here that proxy information
335 for environmental change may be derived, in this case for grain-size variability and the
336 depositional environment for the Dhanchi Island site. Grain-size data was gathered from
337 the Dhanchi Island core samples prior to PXRF analysis, following the methodology of
338 Flood et al. (2015).

339

340 4.3. Data acquisition: Grain-size analysis

341 GSDs were analysed following Flood et al. (2015) using a MalvernMastersizer 2000
342 instrument. Data were aggregated into quarter phi intervals (ϕ scale) over the range of
343 0.02 – 2000 μm , following collection of measurements from the instrument. The centred

344 log-ratio transformation (clr-transformation) was implemented on all grain-size classes
345 with any zero-valued bins of quarter phi intervals removed (i.e., where entire column
346 vectors consisted of 0 row values). Classes of the grain-size distribution containing a zero
347 in any of the observations (i.e., columns where only some of the row values are > 0),
348 were amalgamated and the arithmetic mean calculated (cf. Bloemsma et al., 2012). This
349 process was carried out on the 62.50 μm to 2000 μm fraction (i.e., 4.00 ϕ to -1.00ϕ) for
350 the Dhanchi Island GSD data.

351

352 4.3. Data acquisition: ITRAXTM core-scanning

353 Coring was carried out at Dhanchi, Bonnie Camp, and Sajnekhali in November 2011
354 (sites shown in Fig. 2). Three cores (one from each site) were extracted using a motor
355 driven percussion coring device. These cores were analysed using the ITRAXTM core-
356 scanner (Cox Analytical Systems, Mölndal, Sweden) housed at the School of Geography,
357 University College Dublin. This is a non-destructive analytical approach which provides
358 ED-XRF elemental profiles along with optical imagery and micro-density (X-
359 radiography) information (Croudace et al., 2006). The geochemical data were acquired
360 through an ED-XRF spectrometer consisting of a molybdenum cathode (Croudace et al.,
361 2006). The voltage and current of the X-ray source was the 3kW Mo tube set to 30 kV
362 and 50 mA respectively, with a measurement step-size of 300 μm and exposure time of
363 16 seconds. The latter setting was employed for expedience, to provide high-resolution
364 scanning of all the cores (c. 25 m of material length). The element data (table of elements
365 shown in Table 1) were processed using fitting procedures in the Q-Spec spectral analysis
366 package in order to extract the individual elemental intensities from the spectra output

367 (Croudace et al., 2006). Operation of the software involved selecting elements to be
368 extracted from the XRF spectra, with any spurious or unnecessary elemental choices or
369 incorrect fitting parameters adjusted post hoc through a batch-controlled post-processing
370 of the spectra (Croudace et al., 2006). Invalid readings were noted and not employed in
371 any post-hoc processing (i.e., invalid readings were not used in the LRCE). The scan-
372 lengths from each of the cores were 666 cm for Dhanchi-2 (hole-depth of 728 cm), 923.2
373 cm for Bonnie Camp (hole-depth of 1022 cm), and 639.4 cm for Sajnekhali Island (hole-
374 depth of 791 cm). The total number of readings from each core were Dhanchi-2 with $n =$
375 22,129 valid readings from a total output of 22,201 readings (72 invalid readings),
376 Bonnie Camp with $n = 30,517$ valid readings from a total output of 30,773 readings (256
377 invalid readings), and Sajnekhali with $n = 23,822$ valid readings from a total output of
378 24,201 (379 invalid readings).

379 The LRCE was applied to the global discrete sampling dataset collected ($n=568$)
380 with the model then unfolded onto the elemental data from the high-resolution ITRAX™
381 ED-XRF ($n=76,468$). The alpha (α) and beta (β) slope and intercept regression
382 parameters derived from the LRCE were used to predict the relative concentration of a
383 sub-composition of elements (see section 5 results of this study), for this higher
384 resolution dataset.

385

386 4.4. Data acquisition for calibration: portable X-ray fluorescence spectrometry of
387 reference samples

388 Data acquisition using ED-XRF was undertaken using a Bruker S1 TURBO SD portable
389 X-ray fluorescence (PXRF) spectrometer (Bruker Corporation, Massachusetts, USA)

390 consisting of a 10 mm X-Flash® SDD Peltier-cooled detector with a 4-watt (W) X-ray
391 tube consisting of an Ag target and a maximum voltage of 40kV. Analysis was carried
392 out on discrete samples collected from the Dhanchi-2, Bonnie Camp and Sajnekhali
393 Island cores. In order to ascertain major and trace element composition, the elemental
394 suite was generated using two analytical settings for each sample analysed. Major
395 elements were acquired using a vacuum-pumped, low-energy and high current setting of
396 15kV and 55 μ A instrument setting with no filter. The vacuum-pump was used to remove
397 air from between the sampling window and the detector and allowed for improved
398 analysis of the material, in particular increased sensitivity to light major elements, below
399 and including iron (Fe). The other analytical setting was used for trace element analysis
400 and acquired without a vacuum-pump and employed a yellow filter (Ti and Al), high-
401 energy instrument setting of 40kV and 19.60 μ A. With these instrument settings,
402 elemental data are acquired for heavier elements with little sensitivity for those elements
403 below calcium (Ca). The filter used consists of a 0.001" Ti and 0.012" Al and is already
404 present in the instrument. Using the portable XRF, high and low energy data were
405 acquired for each sample. Unknown samples from the Sundarbans were each measured
406 for 16 seconds, with a set of 22 international geochemical reference standards (shown in
407 Table 1) measured for 120 seconds, this was carried out so as to develop a robust
408 calibration line for the PXRF instrument specific calibration. Since the Bruker software is
409 proprietary, a full disclosure and discussion of the calibration routine is not possible in
410 this study (cf. Rowe et al., 2012).

411 The calibration models used in this research depend on the estimation of error of
412 the covariance matrices, where the magnitude of the uncertainty in the measured

413 variables is accounted for (Bloemsma 2015; Weltje et al., 2015). With this in mind, due
414 to lack of *a priori* knowledge concerning these uncertainties, replicated analysis is
415 required in order to estimate these uncertainties (Bloemsma 2015). Repeated
416 measurements were carried out on a total of 9 samples (3 per core) with 30 additional
417 measurements on each of these samples (n = 270 repeated measurements in total) using
418 the portable ED-XRF.

419

420 4.5. Data acquisition – portable ED-XRF spectra calibration

421 The raw spectra obtained from the Bruker S1 TURBO SD portable ED-XRF require a
422 calibration to convert the data into quantitative weight percentages. The calibration for
423 the portable ED-XRF unit is matrix-specific, so a calibration for major and trace elements
424 of sediments and soils was developed using a suite of 22 reference materials. The
425 calibration of the ED-XRF spectra was carried out using the Bruker AXS calibration
426 software S1CalProcess Version 2.2.32 with the reference concentrations for the low and
427 high energy calibrations produced for each element being evaluated against the
428 concentration of the element as derived from the slope and baseline corrected peak
429 heights. Linear regression analysis of the elemental concentrations quoted by the
430 manufacturers for the international geochemical reference standards are examined along
431 with elemental composition derived from the Bruker AXS S1CalProcess.

432

433 **5. RESULTS**

434 The results presented in this section reflect the data processing and outline how the LRCE
435 was applied to the integrated core-scan ED-XRF data along with the discrete samples

436 analyzed using conventional ED-XRF and grain-size analysis. The LRCE model depends
437 on comparability of the intensity measured elemental composition (i.e., data from the
438 core-scan ITRAX™ data) along with the % elemental composition (i.e., conventional
439 XRF data) a sub-composition of the elements were examined for these modelling
440 purposes.

441 The LRCE model was applied to all of the integrated core-scan samples from the
442 cores. These input data consisted of the total sample population from the three cores
443 (Dhanchi, $n = 163$; Bonnie Camp, $n = 228$; Sajnekhali, $n = 176$; with a total sample
444 population, $n = 567$) with fifteen outliers removed. These outliers were removed as they
445 deviated substantially from the general spread of data points and would bias the
446 prediction of the model. Fig. 4 shows the cross plot of results from the closed, inverse
447 transformed sub-composition of elements with calcium (Ca), iron (Fe), and potassium
448 (K) depicted in the top row (a-c) and rubidium (Rb), titanium (Ti), and zirconium (Zr)
449 shown in the bottom row (d-f). The conventional weighted (reference) ED-XRF
450 composition is on the x-axis with the integrated ITRAX™ derived intensity (predicted)
451 ED-XRF on the y-axis.

452 The lack of a full suite of elemental output is due to the fact that the majority of
453 these elements correspond to the lower energy, and thus atomically lighter, end of the
454 spectrum with poorer excitation efficiency and detection. Data derived from these lighter
455 elements are more difficult to calibrate as there tend to be more peak-overlaps. Finally, as
456 the penetration depth of ED-XRF for the light elements (e.g., Si, Al etc.) tends to be ~
457 hundreds of μm , there is a risk of not actually measuring sediment (i.e., with core scan
458 derived ED-XRF, it is possible to measure water pooled under the Mylar® polyester

459 film). The efficacy of the LRCE is illustrated in Fig. 4, where data appears to be well
460 spread along the model, with calcium, iron and titanium representing the best spread of
461 data points. There appears to be some bias in the potassium modelled output where a
462 number of sample points deviate from the model. This bias may be attributed to the
463 measurement of potassium in ED-XRF (both core-scan and conventionally derived ED-
464 XRF), where potassium appears close to calcium and in some cases there may be some
465 peak overlap if the count time is low (Bloemsma 2015). However, given that the
466 potassium is spread along the x-axis of the known weighted elemental composition, such
467 an artefact of analysis may be attributed to the conventional ED-XRF. Rubidium data
468 points appear to be spread across the regression and derive a reduced correlation. There is
469 also a clustering of the data points from the regression model applied to zirconium.

470 The calibration coefficients, α and β , for the LRCE model are shown in Table 2
471 and Table 3, respectively. These coefficients can be considered to reflect the matrix effect
472 (i.e., scattering, absorption and enhancement effects introduced during measurement,
473 caused by the presence of other elements) and detection efficiency (i.e., sensitivity of the
474 ED-XRF data after pre-processing) in a single-element from ED-XRF derived output
475 (Weltje and Tjallingii, 2008). The LRCE removes the specimen effects, which relate to
476 the deviations of measurement from ideal conditions, however not all of these effects are
477 fully removed (Weltje and Tjallingii, 2008). The α and β regression parameters reflect
478 physical parameters such as grain-size, core-surface elevation, and water content (Weltje
479 and Tjallingii, 2008), and are the main criteria used in the LRCE for calculating the best
480 model fit for each of the elements (i.e., what is the 'best' log-ratio denominator for each
481 of the elements in the dataset) (Weltje and Tjallingii, 2008).

482 In Table 4 and Table 5 the residual variances of the regression and prediction of
483 the dataset used in the LRCE are shown. The residual variance refers to noise as it does
484 not correlate with the compositional variations in a specimen (Bloemsma, 2010). This
485 variance is quantified by taking a clr-transformation of a set of measurements from the
486 same core-locations (i.e., replicate measurements) with the Euclidean distance between
487 the observations measured in order to calculate error estimation (Bloemsma, 2010). Thus,
488 the residual variance effectively quantifies the level of relative ‘noise’ that may be
489 derived from the regression and prediction. The residual variance for both the regression
490 and prediction reveal that calcium accounts for the most consistent variance.

491 The α and β parameters from the log-ratio transformed dataset shown in Fig. 5 (a-
492 e) with Ca found to be the best fitting denominator for Fe, K, Rb, Ti, and Zr. The R^2
493 values of goodness-of-fit in the LRCE denominator are shown in Table 6. The non-
494 linearity found in the original back-transformed data (Fig. 5, Rb and Zr) along with bias
495 (Fig. 5, K) is now removed. Ca is found to be the optimal denominator using the
496 Aitchison distance between the predicted and reference composition. Table 4 shows the
497 median variances and Table 5 depicts the 95% confidence limits corresponding to these
498 residual variances. The non-linearity introduced by the matrix effects has been greatly
499 reduced with log-ratio intensities now distributed linearly with the log-ratio relative
500 concentration (cf. Weltje and Tjallingii, 2008). As a consequence, the elemental
501 concentration can now be derived from any of the intensity observations based on the
502 linear model (black line intersecting the point clouds in Fig. 5) (cf. Weltje and Tjallingii,
503 2008).

504 Using the residual variance of the prediction and the regression (Table 4 and
505 Table 5), the sub-composition closure of the high-resolution dataset from the ITRAX™
506 ED-XRF has been estimated from the lower resolution calibration dataset. As a result, it
507 is now possible, through the calibrated intensity derived ED-XRF with the weighted ED-
508 XRF, to interpolate the high resolution intensity ED-XRF.

509 Shown in Fig. 6a is the PLS model output for the Dhanchi Island core with the
510 PLS-coefficients of c. 0.3 for grain-size depicted by negative values corresponding to the
511 coarse-clay to coarse-silt size fractions. Positive PLS coefficients of c. +0.3 are indicated
512 by coarse-silt to sand sized. The PLS-scores for grain-size indicate positive score
513 fluctuations appear to correspond to coarser sediment coefficients with negative scores
514 found to correspond to that of finer sediment coefficients. The PLS-coefficients for
515 geochemistry (Fig. 6b) show positive values for zirconium and calcium, with the highest
516 negative values found for iron, potassium, rubidium, and titanium. Calcium and
517 zirconium indicate the highest PLS coefficients at c. 0.4 and 0.3 respectively. In contrast,
518 iron, potassium, rubidium and titanium are negatively correlated with PLS-coefficient
519 values of between -0.3 and -0.4. The PLS-scores show a decline in grain-size with a
520 concomitant decline in PLS-scores for geochemistry (calcium and zirconium) (Fig. 6c &
521 d). Furthermore there is an apparent trend found in the PLS-scores for grain-size, firstly a
522 trend consisting of a form of oscillation taking place from c. 787 cm to 491 cm that is
523 superseded by a second trend of PLS-score decline. These trends in light of the PLS-
524 scores may be interpreted as a form of grain-size variability, in which oscillations in
525 grain-size appear to correlate with oscillation in zirconium, while a decline in zirconium
526 is reflected in a decline in grain-size. When the PLS-data are considered along with the

527 PC1-scores and PC1-coefficients for residual geochemistry (Fig. 6e & f), it is evident that
528 throughout the Dhanchi Island core there is a consistent decline of calcium taking place.
529 This can be discerned through the PC1-coefficients for residual geochemistry which
530 depict positive values driven most strongly by calcium at c. 0.7 with negative values
531 being concomitantly driven by zirconium at just over -0.6. Furthermore, negative PC1-
532 coefficient values may be discerned for the rubidium and titanium compositions, with
533 potassium and iron represented by positive coefficient values.

534

535 **6. DISCUSSION**

536 6.1 Reconstructing Late Holocene environmental change from sediments in the West
537 Bengal Sundarbans, India

538 The objective of the study is to investigate how the application of LRCE & PLS to
539 Holocene sediments of a Delta environment can improve interpretation of geochemical
540 indicators of grain-size variability. The geochemistry derived from the application of the
541 LRCE to Holocene sediments in the present study illustrates the efficacy of these subset
542 of elements as useful indicators of environmental change. The LRCE shows that, in the
543 case of the Sundarbans, K, Rb, Fe, Ti, Zr, and Ca can be calibrated, with Ca found to be
544 the best-fit denominator. The utility of these elements for interpreting environmental
545 change within the Sundarbans can be explored by examining the Dhanchi Island core and
546 how these calibrated data may be employed in order to interpret the depositional
547 environment through grain-size variability. However, in order to understand the data
548 generated in this study, there is a requirement to place into the context the key aspects of
549 deltaic environments and how these aid in the interpretation of facies variability derived

550 through the LRCE & PLS models for the case study of the Dhanchi Island core. The role
551 of this discussion is to outline a potential set of circumstances that may characterise a
552 depositional model for this particular site in the Sundarbans.

553

554 6.2 Use of Sundarbans elemental log-ratios as environmental proxies

555 River deltas develop as coastal ‘protuberances’ as a result of high sediment availability
556 with variability in ocean hydrodynamics and localised coastal progradation (cf. Elliott,
557 1986; Wright, 1978; Hanebuth et al. 2012). A dynamic relationship exists in terms of
558 laterally graded intensity between sediment discharge along defined channels
559 counterbalanced with the influence of tides, waves and longshore currents (Hanebuth et
560 al., 2012). Differentiation of external forces in this manner leads to more diverse
561 organisation of deltaic environments that are more locally segmented and temporally
562 complex (Hanebuth et al., 2012). This study attempts to apply this approach to
563 considering the Sundarbans in this manner of localised variability in terms of sedimentary
564 deposition as opposed to applying a generalised model over the entirety of the Ganges-
565 Brahmaputra delta. Modern Holocene delta development is understood to have
566 commenced between 9 and 7.5 cal ka BP associated with the deceleration of sea-level
567 rise (Stanley and Warne, 1994). In terms of sediment supply, it has been found that the
568 occurrence of coastal-shelf deposits, are indicative of the provenance of sediment (Gao
569 and Collins, 2014). If the supply of sediment is ‘small’, then the seabed may consist only
570 of bedrock, relict sediment or reworked materials, this is known as “sediment starved”
571 (Gao and Collins, 2014, pp. 270). Conversely, thick Holocene deposits covering a large
572 area are indicative of an abundant supply of sediment (Gao and Collins, 2014). Sediment

573 supply is principally provided by rivers, and dependent on geographical variability at the
574 global scale (Milliman and Farnsworth, 2011). Grain-size compositions examined with an
575 experimental microdelta by Endo et al. (1996) have found that these compositions are
576 strongly controlled by the textural composition of source sand, analogous to a real-world
577 river system. These results indicate that textural composition of a depositional system is
578 primarily determined by the textural composition of sediment input (Swift et al., 1971;
579 Liu et al., 2000). With this the observed grain-size variability are a result of the transport
580 and deposition processes of sediment delivery to a system, with subsequent reworking of
581 sediments already deposited (Liu et al., 2000). Thus, the nature and amount of sediment
582 input can therefore determine the textural characteristics of a depositional system in
583 receipt of these sediments (Liu et al., 2000). It is now possible to fully consider the data
584 from the Dhanchi Island core and what may be gleaned from the geochemical and grain
585 size variability found and how these fit into the present understanding of deltaic
586 environments.

587 The calcium variability in the Dhanchi Island sediments may therefore be
588 understood as declining from a depth of approximately 500 cm to the core surface. This
589 decline in calcium with the subsequent increase in zirconium, titanium, potassium, and
590 rubidium composition may be interpreted as terrestrial sediment flux with diminished
591 marine deposition. This calcium signal is pervasive in the four log-ratio pairs and does
592 not appear to lend to the interpretation of grain size variability per se in the depositional
593 characteristics of the Dhanchi Island site. It may be discernible that terrestrial sediment
594 flux appears to be uncorrelated with calcium, thus, sediment provenance for the fine and
595 coarse sediment appears to be independent of a marine or a tidally driven source.

596 In this context, the Dhanchi Island sediments exhibit a predisposition to
597 terrigenous sediments, in agreement with Rogers et al. (2013) that geographical distance
598 is not necessarily a limiting factor on sedimentation taking place (assuming the
599 predominance of terrigenous sediment in the Dhanchi Island sediments). One of the key
600 trends in all of these log-ratio pairs with calcium as the denominator, is that there appears
601 to be a non-stationarity signal present, in which although the variability between log-ratio
602 values appears to indicate some form of oscillation throughout the sequence, in each log-
603 ratio pair however the overall behaviour as noted is an increase in the numerator value at
604 the expense of the calcium denominator (Fig. 7). Non-stationary signals, in the case of
605 these log-ratio pairs, implies that the depositional processes taking place are drifting in
606 time, in particular the increase in zirconium relative to calcium may be derived from the
607 aggradation of the island surface.

608 Grain size variation delivered by rivers has also been found to become finer in the
609 seaward direction and this is more pronounced in an aggradational environment
610 (Dalrymple and Choi, 2007). However, given that this part of the Sundarbans is an
611 'abandoned' deltaic-estuarine site, it may be classed as being part of the 'middle estuary'
612 which occupies effectively the same environmental location within an estuary as active
613 delta-plain distributary channels within a delta (Dalrymple and Choi, 2007). In terms of a
614 deltaic system such an abandoned set of distributary channels are thought of as estuarine
615 due to the fact that they do not carry as much river discharge and also experience
616 reworking by tidal currents (Dalrymple, 2006; Dalrymple and Choi, 2007). These areas
617 experience net landward transportation of sediment from the seaward margin, which is
618 contrast to that of active delta channels that experience a reverse (Dalrymple and Choi,

619 2007). It has also been noted that in terms of evidence for river action in the physical
620 structures present, there tends to be almost no evidence for seasonality in fluvial
621 discharge (Dalrymple and Choi, 2007). Along with this, there tends to be a case in
622 abandoned channels of such delta plain estuaries that sediments from somewhat older
623 distributary-mouth-bar deposits experience reworking within these systems (Dalrymple
624 and Choi, 2007). The overarching presence of silt and clay would suggest a muddy
625 depositional environment.

626 As identified by Goodbred and Saito (2011) such environments are generally
627 made of what are termed 'sand-mud alterations' consisting of flaser, lenticular and wavy
628 laminations or bedding. Furthermore, such tidal flat environments are composed of
629 bidirectional sedimentary structures such as sand-layer stacking, cross-laminations, mud-
630 drapes, and potentially, double mud-drapes (Goodbred and Saito, 2011). These
631 depositional features are usually indicative of tidal depositional constraints on a
632 sedimentary system (Goodbred and Saito, 2011). In this regard, although such
633 sedimentary structures are difficult to discern from a discrete number of grain size
634 samples, it is possible to elucidate such a depositional environment, potentially through
635 high-resolution core-scanning as shown in Fig. 7. However, without having a robust
636 chronology, it is still difficult to discern such tidal sedimentary structures. In a study of
637 grain size characteristics of tidal-bore deposition in the Qiantang Estuary by Fan et al.
638 (2014), GSDs are found to be composed of a principal coarse and secondary fine
639 component. The modal size, sorting, and proportions found in these coarse and fine
640 components are ascribed to different depositional processes on the tidal flats (Fan et al.,

641 2014). Sandy laminae were found to be well sorted compared to those of muddy laminae,
642 reflecting disparate depositional stages of waning flow and slack tides (Fan et al., 2014).

643 The dominant, upward-fining in GSDs as shown in Fig. 6 & 7 may be attributed
644 to what Dalrymple et al. (1992) refer to as 'lateral shifting of channel bedforms'. Such
645 lateral shifting leads to this trend in grain size as currents tend to be higher at greater
646 depths and weaker when over bar crests (Dalrymple et al., 1992). These fining-up
647 sequences comprising muddy tidal flats may actually cap subtidal sand ridges (Wells,
648 1995). A similar model of facies succession has been proposed by Goodbred and Saito
649 (2011), where the migration of tidal channels and creeks across tidal flats, contribute to
650 this fining up facies succession. The clay fraction elucidated from the first and second
651 principal components may represent the mud-drapes and fluid-muds which may be
652 attributed to slack water or poor water flows (cf. Wells, 1995).

653 In Marine sediments, the element profile of Ca is generally considered to reflect
654 the predominant abundance of biogenic calcite (Arz et al., 1998; Tjallingii et al., 2010).
655 There is known to be poor preservation of CaCO_3 in the Sundarbans progradational lower
656 delta plain sequence relative to the marsh and mangrove deposits of other deltaic systems
657 around the world (Allison et al., 2003).

658 There appears to be greater agreement found between sediment provenance
659 proposed by Rogers et al. (2013) and sediment depositional model outlined here in terms
660 of distal sediment transport from fluvial sources, reflected in the log-ratio pairs discussed.
661 The non-stationary signals found in elemental log-ratio pairs may be attributed to tidal
662 processes in the manner described by Dalrymple and Choi (2007). However, what is
663 further elucidated through the joint geochemical and grain-size analysis approach is tha

664 the Sundarbans, through the Dhanchi Island example presented in this study reflects a
665 locally segmented & temporally complex system that does not fall into a singular regime
666 classification given the complex relationship that is exhibited by tidal variability
667 (Hanebuth et al., 2012). Furthermore, although sediments may undergo reworking, what
668 has been found is a predominantly terrestrial source for sediments present in the
669 Sundarbans; this does not fit closely with the implication that the Sundarbans are
670 'sediment starved' as outlined by Gao and Collins (2014). Rather, geographically
671 (Milliman and Farnsworth, 2011) and climatically (Liu et al., 2000; Gao and Collins,
672 2014) variable processes operate in producing a complex depositional environment.
673 Sedimentary facies variability in the form of tidal processes can only be inferred in this
674 study by the diminished calcium variability found. These tidal processes do not appear to
675 operate in isolation and may be coupled to some form of monsoonal variability in the
676 manner proposed by Liu et al. (2000) for Asia and by Rogers et al. (2013) more
677 specifically applied to the Sundarbans.

678 The utility of these calibrated geochemical proxies from the Sundarbans is
679 illustrated in Fig. 7 from the Dhanchi Island core. Through plotting the log-ratio pairs
680 there appears to be some oscillating trend throughout the core, in particular with log-
681 transformed Zr and Rb (see Fig. 7). There is a steady decline in Zr nearer to the top of the
682 core (from a depth of 450 cm to the core surface). This indicates a decline in zirconium,
683 and potentially an increase in rubidium. It is only through CoDa however that such a
684 trend can be illustrated in the first place as ratios by themselves possess the undesirable
685 property of asymmetry, meaning that conclusions based on evaluation of the ratio of two
686 elements (e.g., A/B), cannot be directly translated into equivalent statements about B/A

687 (Weltje, 2012; Weltje et al., 2015). Taking this approach further, the Rb and K log-
688 transformed data shown in Fig. 7, appear to reflect the trend found in rubidium and
689 zirconium; with an oscillating trend throughout the core. However, there does not appear
690 to be any discernible increase or decrease in rubidium up core, with the log-ratio data
691 remaining somewhat unvarying.

692 The overarching trend would suggest a strong relationship between zirconium and
693 coarse grained sediment, as these sites are considered to reflect upward fining sequences
694 (e.g., Allison et al., 2003; Flood et al., 2015). In particular the trend consists of
695 coarse/very coarse-silt and sand with a concomitant relationship between coarse clay and
696 medium/coarse-silt for rubidium. Furthermore, the variability of rubidium with potassium
697 would suggest an unvarying relationship between the fine-grained sediments. This might
698 indicate that fine-grained provenance is tied to rubidium and potassium, with coarse
699 grained sediment provenance strongly linked to zirconium. Ca geochemistry (shown in
700 Fig. 6 & 7) may be linked to some external environmental control, such as sea-level or
701 tidal inundation as calcium is generally only present in liquid form in the marine
702 environment. Ca appears to correlate negatively with Zr, Ti, K, and Rb in the Dhanchi
703 Island core. This decline in Ca with concomitant increases in Zr, Ti, K, and Rb (Fig. 7)
704 may be interpreted as reflecting terrestrial derived sediment flux with diminished marine
705 or carbonate deposition (or at least a marine source of variability). Terrestrial sediment
706 flux therefore appears to be uncorrelated with Ca, implying that sediment provenance is
707 independent of a marine or tidally driven source.

708

709 **7. CONCLUSION**

710 Through CoDa it has been possible to calibrate core-scan derived XRF data, and produce
711 useful elemental proxies for analysing a clastic sedimentary environment. When using the
712 LRCE calibration model coefficients to examine such clastic sedimentary environments
713 in the Indian Sundarbans quantified data outputs are possible, and combined with grain-
714 size data a broader understanding of the depositional environment is possible. The lack of
715 a full elemental suite, attributed to a poorer linear fit between weighted concentration and
716 intensity data, does not detract from the approach to XRF core-scan calibration. The
717 elements that have been calibrated through the LRCE in this study may be used to
718 demonstrate provenance (e.g., Zr, Rb, Ti, etc.) and processes of sedimentation (e.g., Ca)
719 in this area of the G-B delta. Ca has been found to be the optimum log-ratio denominator,
720 and when examined in a log-ratio framework, it may be used to distinguish between
721 marine-terrestrial sediment fluxes in a high-resolution XRF dataset. Grain-size variability
722 modelled with calibrated geochemistry has shown that Zr and Rb are interpreted as robust
723 proxies for coarse and fine sediment deposition, respectively. A potential sedimentary
724 facies model for the Sundarbans through the PLS modelling approach allows
725 investigators to incorporate both depositional and provenance variability. Future research
726 should focus on building a more constrained calibration model for the G-B delta, with
727 more sedimentary cores from different facies sequences and employing other
728 geochemical analyses tools (e.g., ICP-OES/MS). The LRCE & PLS approaches applied
729 in this study for calibration of sediments represent a robust application of the principles
730 of CoDa, and it is recommended that future studies in the G-B delta and other delta
731 environments should seek to refine core-scanning XRF and grain-size analysis in light of
732 the approaches outlined in this study.

733 **ACKNOWLEDGEMENTS**

734 RPF acknowledges the support provided by a Research Studentship from the Department
735 for Employment and Learning (Northern Ireland) and the Department of Education and
736 Science's Higher Education Grant Scheme (ROI) provided through Laois County Council
737 (ROI). RPF also acknowledges the School of Geography, Archaeology and
738 Palaeoecology (GAP), Queen's University, Belfast (QUB) for the fieldwork support
739 provided by their Soulby Research Fund. RPF acknowledges the assistance and technical
740 support provided by Mike Dobby (formerly of Bruker Instruments UK Ltd.), John
741 Meneely and Patricia Warke (QUB), Ciara Fleming, Clare Ní Cholmáin, and David
742 Colgan (UCD). The authors would like to thank the three anonymous reviewers for the
743 constructive comments and help in improving the quality of this manuscript.

744

745 **Reference list**

- 746 Aitchison, J., 1982. The statistical analysis of compositional data (with discussion). *J. R.*
747 *Stat. Soc. Ser. B* 44, 139–177.
- 748 Aitchison, J., 1986. *The Statistical Analysis of Compositional Data*. Chapman and Hall,
749 London. 416 pp.
- 750 Allison, M.A. 1998a. Geologic framework and environmental status of the Ganges-
751 Brahmaputra delta. *Journal of Coastal Research* 14, 826–836.
- 752 Allison, M.A., 1998b. Historical changes in the Ganges-Brahmaputra delta. *Journal of*
753 *Coastal Research* 14, 1269–1275.

- 754 Allison, M.A., Khan, S.R., Goodbred Jr., S.L., Kuehl, S.A., 2003. Stratigraphic evolution
755 of the late Holocene Ganges-Brahmaputra lower delta plain. *Sedimentary Geology*
756 155, 317–342.
- 757 Arz, H.W., Patzold, J., Wefer, G., 1998. Correlated millennial-scale changes in surface
758 hydrography and terrigenous sediment yield inferred from last-glacial marine
759 deposits off Northeastern Brazil. *Quaternary Research* 50, 157–166.
- 760 Bhattacharyya, S., Pethick, J., Sensarma, K. 2013. Managerial response to sea level rise
761 in the tidal estuaries of the Indian Sundarban: a geomorphological approach. In
762 Xun, W., Whittington, D. (Eds.) *Water Policy Journal: Special Edition: The*
763 *Ganges. Basin Water Policy* 15, pp. 51–74.
- 764 Bird, E.F.C., 1984. *Coasts: an introduction to coastal geomorphology*. Blackwell, Oxford,
765 320 pp.
- 766 Bjørlykke, K., 2010. Chapter 3 Sedimentary Geochemistry: How Sediments are
767 Produced. In Bjørlykke, K. (ed.). *Petroleum geoscience: From sedimentary*
768 *environments to rock physics*. Heidelberg, Springer, 508 pp.
- 769 Bloemsmā, M.R. (2010) *Semi-Automatic Core Characterisation based on Geochemical*
770 *Logging Data*, Unpublished M.Sc. thesis: Delft University of Technology, The
771 Netherlands, 164 pp.
- 772 Bloemsmā, M.R. (2015) *Development of a Modelling Framework for Core Data*
773 *Integration using XRF Scanning*, Unpublished Ph.D. thesis: Delft University of
774 Technology, The Netherlands, 229 pp.

- 775 Bloemsmā, M.R., Zabel, M., Stuu, J.B.W., Tjallingii, R., Collins, J.A., Weltje, G.J.
776 (2012) 'Modelling the joint variability of grain-size and chemical composition in
777 sediments', *Sedimentary Geology*, 280, pp. 135-148.
- 778 Croudace, I.W., Rindby, A., Rothwell, R.G., 2006. ITRAX: description and evaluation of
779 a new multi-function X-ray core scanner. In: Rothwell, R.G. (Ed.), *New
780 Techniques in Sediment Core Analysis*. Special Publication, vol. 267. Geological
781 Society, London, pp. 51–63.
- 782 Dalrymple, R.W. and Choi, K., 2007. Morphologic and facies trends through the fluvial–
783 marine transition in tide-dominated depositional systems: a schematic framework
784 for environmental and sequence-stratigraphic interpretation. *Earth-Science Reviews*
785 81, 135–174.
- 786 Dalrymple, R.W., 2006. *Incised Valleys in Time and Space: An Introduction to the
787 Volume and An Examination of the Controls on Valley Formation and Filling*. In:
788 Dalrymple, R.W., Leckie, D.A., Tillman, R.W. (Eds.), *Incised Valleys in Time and
789 Space*. SEPM (Society for Sedimentary Geology) Special Publication 85, pp. 5–12.
- 790 Dalrymple, R.W., Zaitlin, B.A., and Boyd, R., 1992. Estuarine facies models: conceptual
791 basis and stratigraphic implications. *Journal of Sedimentary Petrology*, 1130-1146.
- 792 de Jong, S., 1993. SIMPLS: an alternative approach to partial least squares regression.
793 *Chemometrics and Intelligent Laboratory Systems* 18, 251–263.
- 794 De Vries, J.L., Vrebos, B.A.R., 2002. Quantification of infinitely thick specimens by
795 XRF analysis. In van Grieken, R.E., Markovicz, A.A. (Eds.), *Handbook of X-Ray
796 Spectrometry*, Second Edition. Marcel Dekker, New York, pp. 341–405.

- 797 Elliott, T., 1986. Deltas. In: Reading, H.G. (Ed.), *Sedimentary Environments and Facies*.
798 Blackwell Scientific, Oxford, pp. 113–154.
- 799 Endo, N., Masuda, F., Yokokawa, M., 1996. Grain-size distributions of sediment carried
800 by single transportation modes in an experimental microdelta system. *Sed. Geol.*
801 102, 297–304.
- 802 Fan, D.D., Tu, J.B., Shang, S., Cai, G.F., 2014. Characteristics of tidal-bore deposits and
803 facies associations in the Qiantang Estuary, China. *Marine Geology*, 348, 1–14.
- 804 Flood, R.P., Orford, J.D., McKinley, J.M., Roberson, S., 2015. Effective grain-size
805 distribution analysis for interpretation of tidal–deltaic facies: West Bengal
806 Sundarbans. *Sedimentary Geology*, 318, 58–74.
- 807 Gao, S. and Collins, M.B., 2014. Holocene sedimentary systems on continental shelves.
808 *Marine Geology*, 352, 268–294.
- 809 Goodbred Jr., S.L., Kuehl, S.A., 2000. The significance of large sediment supply, active
810 tectonism and eustasy on margin sequence development: Late Quaternary
811 stratigraphy and evolution of the Ganges-Brahmaputra delta. *Sedimentary Geology*
812 133, 227–248.
- 813 Goodbred Jr., S.L., Saito, Y., 2012. Tide-dominated deltas. In: Davis, R.A., Dalrymple,
814 R.W. (Eds.), *Principles of Tidal Sedimentology*. Springer Science + Business
815 Media B.V, pp. 129–149.
- 816 Hanebuth, T.J., Proske, U., Saito, Y., Nguyen, V.L. and Ta, T.K.O., 2012. Early growth
817 stage of a large delta—Transformation from estuarine-platform to deltaic-
818 progradational conditions (the northeastern Mekong River Delta, Vietnam).
819 *Sedimentary Geology*, 261, 108–119.

- 820 Jansen, J.H.F., Van der Gaast, S.J., Koster, B., Vaars, A.J., 1998. CORTEX, a shipboard
821 XRF scanner for element analyses in split sediment cores. *Quat. Res.* 151, 143–153.
- 822 Jenkins, R., 1999. *X-Ray Fluorescence Spectroscopy*, Second Edition. Wiley & Sons,
823 New York. 207 pp.
- 824 Kendall, M.G., Stuart, A., 1973. *The Advanced Theory of Statistics, Volume 2: Inference*
825 *and Relationships*. Griffin, London.
- 826 Liu, J.T., Huang, J.S., Hsu, R.T. and Chyan, J.M., 2000. The coastal depositional system
827 of a small mountainous river: a perspective from grain-size distributions. *Marine*
828 *Geology*, 165, 63-86.
- 829 Liu, J.T., Huang, J.-S., Hsu, R.T., Chyan, J -M., 2000. The coastal depositional system of
830 a small mountainous river: a perspective from grain-size distributions. *Marine*
831 *Geology* 165, 63–86.
- 832 Liu, J.T., Zarillo, G.A., 1989. Distribution of grain sizes across a transgressive shoreface.
833 *Mar. Geol.* 87, 121–136.
- 834 Liu, J.T., Zarillo, G.A., 1990. Shoreface dynamics: evidence from sediment patterns and
835 bathymetry. *Mar. Geol.* 94 (1/2), 37–53.
- 836 Milliman J D, Farnsworth K L, 2011. *River discharge to the coastal ocean: a global*
837 *synthesis*. Cambridge University Press, Cambridge, 384 pp.
- 838 Milliman, J.D., Syvitski, J.P.M., 1992. Geomorphic/tectonic control of sediment
839 discharge to the oceans: the importance of small mountain rivers. *Journal of*
840 *Geology* 100, 525-544.

- 841 Nesbitt, H.W., Young, G.M., 1984. Prediction of some weathering trends of plutonic and
842 volcanic rocks based on thermodynamic and kinetic considerations. *Geochimica et*
843 *Cosmochimica Acta* 48, 1523-1548.
- 844 Potts, P.J., 1987. *Handbook of Silicate Rock Analysis*. Blackie, Glasgow. 622 pp.
- 845 Press, W.H., Teukolsky, S.A., Vetterling, W.T., Flannery, B.P., 1994. *Numerical Recipes*
846 *in FORTRAN: The Art of Scientific Computing*, Second Edition. University Press,
847 Cambridge. 963 pp.
- 848 Ramsey, M.H., Potts, P.J., Webb, P.C., Watkins, P., Watson, J.S., Coles, B.J., 1995. An
849 objective assessment of analytical method precision: comparison of ICP-AES and
850 XRF for the analysis of silicate rocks. *Chem. Geol.* 124, 1–19.
- 851 Richter, T.O., Van der Gaast, S., Koster, B., Vaars, A., Gieles, R., De Stigter, H., De
852 Haas, H., van Weering, T.C.E., 2006. The Avaatech XRF core scanner: technical
853 description and applications to NE Atlantic sediments. In: Rothwell, R.G. (Ed.),
854 *New Techniques in Sediment Core Analysis*. Special Publication, vol. 267.
855 Geological Society, London, pp. 39–50.
- 856 Rogers, K.G., Goodbred Jr., S.L., Mondal, D.R., 2013. Monsoon sedimentation on the
857 ‘abandoned’ tide-influenced Ganges-Brahmaputra delta plain. *Estuarine, Coastal*
858 *and Shelf Science* 131, 297–309.
- 859 Rothwell, R.G., Hoogakker, B., Thomson, J., Croudace, I.W., Frenz, M., 2006. Turbidite
860 emplacement on the southern Balearic Abyssal Plain (western Mediterranean Sea)
861 during Marine Isotope Stages 1-3: an application of ITRAX XRF scanning of
862 sediment cores to lithostratigraphic analysis. In: Rothwell, R.G. (Ed.), *New*

- 863 Techniques in Sediment Core Analysis. Special Publication, vol. 267. Geological
864 Society, London, pp. 79–98.
- 865 Rowe, H., Hughes, N., Robinson, K., 2012. The quantification and application of
866 handheld energy-dispersive x-ray fluorescence (ED-XRF) in mudrock
867 chemostratigraphy and geochemistry. *Chemical Geology* 324–325, 122–131.
- 868 Ryan, P., 2014. Environmental and low temperature geochemistry. New York, John
869 Wiley & Sons, 416 pp.
- 870 Salminen, R. (Chief editor). Geochemical atlas of Europe. Part 1: Background
871 information, methodology and maps. EuroGeoSurveys, Espoo, Finland, 2005.
- 872 Stanley, D.J., Warne, A.G., 1994. Worldwide initiation of Holocene marine deltas by
873 deceleration of sea-level rise. *Science* 265, 228–231.
- 874 Swift, D.J.P., Sanford, R.B., Dill, C.E., Avignone, N.F., 1971. Textural differentiation on
875 the shore face during erosional retreat of an unconsolidated coast Cape Henry to
876 Cape Hatteras, western North Atlantic Shelf. *Sedimentology* 16, 221–250.
- 877 Syvitski, J.P.M., Peckham, S. D., Hilberman, R. D., Mulder, T., 2003. Predicting the
878 terrestrial flux of sediment to the global ocean: a planetary perspective.
879 *Sedimentary Geology* 162, 5–24.
- 880 Ta, T.K.O., Nguyen, V.L., Tateishi, M., Kobayashi, I., Saito, Y., 2005. Holocene delta
881 evolution and depositional models of the Mekong River Delta, southern Vietnam.
882 In: Giosan, L., Bhattacharya, J.P. (Eds.), *River deltas — concepts, models, and*
883 *examples: SEPM (Society Economic Palaeontologists Mineralogists) Special*
884 *Publication*, 83, pp. 453–466.

- 885 Tanabe, S., Saito, Y., Vu, Q.L., Hanebuth, T.J.J., Ngo, Q.L., 2006. Holocene evolution of
886 the Song Hong (Red River) delta system, northern Vietnam. *Sedimentary Geology*
887 187, 29–61.
- 888 Thomson, J., Croudace, I.W., Rothwell, R.G., 2006. A geochemical application of the
889 ITRAX scanner to a sediment core containing eastern Mediterranean sapropel units.
890 In: Rothwell, R.G. (Ed.), *New Techniques in Sediment Core Analysis*. Special
891 Publication, vol. 267. Geological Society, London, pp. 65–77.
- 892 Tjallingii, R., 2007. Application and quality of XRF core scanning in reconstructing late
893 Pleistocene NW African continental margin sedimentation and paleoclimate
894 variations. Unpublished PhD thesis: Fachbereich Geowissenschaften Universität
895 Bremen, Germany, 114 pp.
- 896 Tjallingii, R., Stattegger, K., Wetzel, A. and Van Phach, P., 2010. Infilling and flooding
897 of the Mekong River incised valley during deglacial sea-level rise. *Quaternary*
898 *Science Reviews*, 29, 1432–1444.
- 899 Wells, J.T., 1995. Tide-dominated estuaries and tidal rivers. *Developments in*
900 *Sedimentology*, 53, pp.179-205.
- 901 Weltje, G.J., 2012. Quantitative models of sediment generation and provenance: State of
902 the art and future developments. *Sedimentary Geology*, 280, 4-20.
- 903 Weltje, G.J., Bloemsmma, M.R., Tjallingii, R., Heslop, D., Röhl, U., Croudace, I.W., 2015.
904 Prediction of geochemical composition from XRF-core-scanner data: A new
905 multivariate approach including automatic selection of calibration samples and
906 quantification of uncertainties. In Croudace, I.W., and Rothwell, R.G., (eds.)
907 *Micro-XRF Studies of Sediment Cores: Applications of a non-destructive tool for*

- 908 the environmental sciences. Dordrecht, NL, Springer, 507-534. (Developments in
909 Paleoenvironmental Research, 17).
- 910 Weltje, G.J., Tjallingii, R., 2008. Calibration of XRF core scanners for quantitative
911 geochemical logging of sediment cores: theory and application. *Earth and Planetary
912 Science Letters*, 274(3), 423-438.
- 913 Wright, L.D., 1978. River deltas. In: Davis Jr., R.A. (Ed.), *Coastal Sedimentary
914 Environments*. Springer, New York, pp. 5–68.
- 915 Wold, S., Martens, H., Wold, H., 1982. The multivariate calibration problem in chemistry
916 solved by the PLS method. In: Ruhe, A., Kagstrom, B. (Eds.), *Proc. Conf. Matrix
917 Pencils*. Springer Verlag, Heidelberg, pp. 286–293.
- 918 Yoshida, S., Steel, R.J., Dalrymple, R.W., 2007. Changes in depositional processes — an
919 ingredient in a new generation of sequence-stratigraphic models. *Journal of
920 Sedimentary Research* 77, 447–460.

921

922 List of Tables

- 923 Table 1: Tally of reported values, minimum values, and maximum values of elemental
924 concentrations (%) for the suite of calibration international geochemical reference
925 standards used in the Bruker AXS S1CalProcess calibration software and subsequent
926 LRCE
- 927 Table 2: Alpha (α) LRCE model parameters
- 928 Table 3: Beta (β) LRCE model parameters
- 929 Table 4: Residual variance of regression of Sundarbans dataset
- 930 Table 5: Residual variance of predicted of Sundarbans dataset

931 Table 6: R^2 values of LRCE (Ca R^2 values highlighted in bold, representative of optimum
932 log-ratio denominator) of Sundarbans dataset

933

934 **List of Figures**

935

936 Fig. 1 Extent of the G-B tidal delta complex, (a) West Bengal Sundarbans (India), (b)
937 East Bengal Sundarbans (Bangladesh), and (c) Kuakata Peninsula (Bangladesh) (adapted
938 from Rogers et al., 2013)

939 Fig. 2 Sites cored in the West Bengal Sundarbans, India (November 2010) (after Flood et
940 al., 2015)

941 Fig. 3 Graphical representation of the rationale behind the calibration approach. Further
942 details are provided in the text (adapted from Bloemsmas et al., 2012)

943 Fig. 4 Results of the calibration of the ED-XRF data, with the reference bulk composition
944 (x-axis) and predicted bulk chemistry (y-axis) of discrete samples from the Dhanchi-2,
945 Bonnie Camp, and Sajnekhali Island cores. Calcium (Ca) is shown in (a), iron (Fe) is
946 shown in (b), potassium is shown in (c), rubidium is shown in (d), titanium is shown in
947 (e), and zirconium (Zr) is shown in (f)

948 Fig. 5 Linear fit between log-ratio measured intensities and log-ratio of the reference bulk
949 chemistry with Ca as the optimum log-ratio denominator from the discrete samples of the
950 Dhanchi-2, Bonnie Camp, and Sajnekhali Island cores. Fit of iron and calcium shown in
951 (a), fit of potassium and calcium shown in (b), fit of rubidium and calcium shown in (c),
952 fit of titanium and calcium shown in (d), and fit of zirconium and calcium shown in (e)

- 953 Fig. 6 Partial least squares (PLS) model of grain-size and calibrated geochemistry for the
954 Dhanchi Island core
- 955 Fig. 7 Log-ratio elemental logs from the Dhanchi Island core

International geochemical reference standard	Alternative Reference	Origin	Issuing Body	Description	Accepted values (% concentration) for international geochemical reference standards used in the Bruker AXS S1CalProcess calibration software and subsequent LRCF.						Minimum values (following Mudrock calibration of PXRF)						Maximum values (following Mudrock calibration of PXRF)					
					K	Ca	Ti	Fe	Rb	Zr	K	Ca	Ti	Fe	Rb	Zr	K	Ca	Ti	Fe	Rb	Zr
<i>GSD-1</i>	GBW 07310	China IGGE IRMA	IGGE	Stream Sediment	2.770	4.600	0.980	7.350	0.116	0.310	0.514	4.174	0.567	6.396	0.114	0.324	2.628	4.523	0.870	6.681	0.127	0.334
<i>GSD-2</i>	GBW 07302	China	IGGE	Stream Sediment	5.190	0.250	0.230	1.890	0.470	0.460	3.064	0.405	0.128	3.046	0.477	0.434	5.469	0.438	0.281	3.122	0.510	0.461
<i>GSD-3</i>	GBW 07303	China	IGGE	Stream Sediment	2.460	0.220	1.060	6.510	0.079	0.220	0.689	0.276	0.842	6.194	0.085	0.205	2.626	0.350	1.091	6.878	0.087	0.245
<i>GSD-4</i>	GBW 07304	China	IGGE	Pond Sediment	2.230	7.520	0.890	5.900	0.130	0.188	0.559	6.792	0.522	5.583	0.130	0.178	2.260	7.260	0.828	6.129	0.137	0.195
<i>GSD-5</i>	GBW 07305	China	IGGE	Pond Sediment	2.100	5.340	0.900	5.860	0.118	0.220	0.739	4.937	0.570	5.482	0.115	0.198	2.248	5.386	0.832	6.133	0.120	0.211
<i>GSD-6</i>	GBW 07306	China	IGGE	Stream Sediment	2.440	3.870	0.780	5.880	0.107	0.170	0.745	3.628	0.434	5.590	0.116	0.192	2.425	4.007	0.700	5.915	0.122	0.204
<i>GSD-7</i>	GBW 07307	China	IGGE	Stream Sediment	3.550	1.660	0.750	6.490	0.147	0.162	0.738	1.589	0.484	6.355	0.142	0.157	3.523	1.743	0.764	6.644	0.155	0.178
<i>GSD-8</i>	GBW 07308	China IGGE IRMA	IGGE	Stream Sediment 142308	2.830	0.250	0.310	2.200	0.132	0.490	1.584	0.272	0.509	2.754	0.122	0.454	3.242	0.387	0.686	3.260	0.156	0.504
<i>GSD-9</i>	GBW 01309	China IGGE IRMA	IGGE	Sediment 300603	1.990	5.350	0.920	4.860	0.080	0.370	0.669	5.463	0.565	4.921	0.079	0.360	2.180	5.996	0.847	4.943	0.094	0.375
<i>GSD-10</i>	GBW 07310	China	IGGE	Stream Sediment	0.125	0.700	0.210	3.860	0.009	0.070	0.216	0.722	0.080	3.062	0.010	0.066	0.551	0.915	0.289	4.352	0.016	0.096
<i>GSD-11</i>	GBW 07311	China	IGGE	Stream Sediment	3.280	0.470	0.350	4.390	0.408	0.153	1.354	0.533	0.189	3.497	0.350	0.138	3.313	0.578	0.399	3.692	0.396	0.157
<i>GSD-12</i>	GBW 07312	China	IGGE	Stream Sediment	2.910	1.160	0.250	4.880	0.270	0.234	1.149	1.064	0.070	4.088	0.250	0.207	2.915	1.223	0.291	4.462	0.266	0.235
<i>GSS-1</i>	GBW 07401	China	IGGE	Dark Brown Soil	2.590	1.720	0.810	5.190	0.140	0.245	1.173	1.588	0.620	4.986	0.145	0.252	2.597	1.804	0.854	5.511	0.152	0.276
<i>GSS-2</i>	GBW 07402	China	IGGE	Chestnut Soil	2.540	2.360	0.450	3.520	0.088	0.219	1.586	1.990	0.305	3.771	0.101	0.209	2.710	2.495	0.496	3.893	0.104	0.240
<i>GSS-3</i>	GBW 07403	China	IGGE	Yellow Brown Soil	3.040	1.270	0.370	2.000	0.085	0.246	2.128	1.207	0.316	2.905	0.096	0.275	3.427	1.388	0.453	3.045	0.102	0.313
<i>GSS-4</i>	GBW 07404	China	IGGE	Limy Soil	1.030	0.260	1.800	10.300	0.075	0.500	0.094	0.255	1.568	10.848	0.055	0.418	1.365	0.351	1.874	11.194	0.075	0.463
<i>GSS-5</i>	GBW 07405	China	IGGE	Yellow Red Soil	1.500	0.095	1.050	12.620	0.117	0.272	ND	0.160	0.796	12.240	0.063	0.144	1.774	0.189	1.140	12.979	0.069	0.176
<i>GSS-6</i>	GBW 07406	China	IGGE	Yellow Red Soil	1.700	0.220	0.730	8.090	0.237	0.220	0.517	0.266	0.592	8.941	0.184	0.161	1.955	0.316	0.841	9.236	0.205	0.185
<i>GSS-7</i>	GBW 07407	China	IGGE	Laterite Soil	0.200	0.160	3.360	18.760	0.016	0.318	ND	0.125	2.848	17.128	0.008	0.265	0.594	0.224	3.342	18.074	0.014	0.304
<i>GSS-8</i>	GBW 07408	China	IGGE	Loess	2.240	8.270	0.630	4.480	0.096	0.229	0.790	7.925	0.266	4.433	0.102	0.217	2.481	8.408	0.562	4.827	0.106	0.241
<i>JSD-1</i>		Geological Survey of Japan	GSI	Stream Sediment	2.190	3.070	0.650	5.110	0.065	0.000	1.002	2.769	0.469	5.274	0.077	0.158	2.283	3.063	0.687	5.283	0.084	0.177
<i>MAG-1</i>		U.S. Dept. of the Int. Geo. Survey	USGS-AEG	Marine mud (Gulf of Maine)	3.550	1.370	0.751	6.800	0.149	0.126	1.412	0.369	0.266	3.958	0.149	0.114	2.971	0.531	0.625	4.476	0.173	0.136

ND: No data

	Ca	Fe	K	Rb	Ti	Zr
Ca	0	0.8436	0.8486	0.9553	0.8735	0.8917
Fe	0.8436	0	1.2911	-10.2447	0.5525	0.8518
K	0.8486	1.2911	0	27.9561	6.2592	1.1371
Rb	0.9553	-10.2447	27.9561	0	42.3024	1.2566
Ti	0.8735	0.5525	6.2592	42.3024	0	1.1717
Zr	0.8918	0.8518	1.1371	1.2566	1.1717	0

ACCEPTED MANUSCRIPT

	Ca	Fe	K	Rb	Ti	Zr
Ca	0	1.626	-0.4527	0.8188	0.7702	0.082
Fe	-1.626	0	-3.5275	51.179	0.1718	-1.5035
K	0.4527	3.5275	0	-37.787	-0.445	-0.0172
Rb	-0.8188	-51.179	37.787	0	46.9791	-1.0694
Ti	-0.7702	-0.1718	0.4449	-46.9791	0	-1.2133
Zr	-0.082	1.5035	0.01717	1.0694	1.2133	0

ACCEPTED MANUSCRIPT

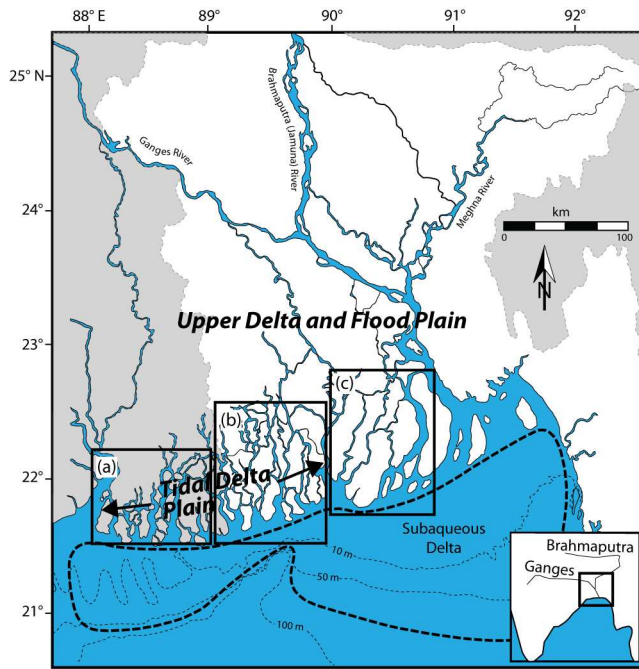
	Ca	Fe	K	Rb	Ti	Zr
Ca	0	0.00945	0.00793	0.01423	0.00697	0.01032
Fe	0.00945	0	0.00192	0.00872	0.00167	0.01209
K	0.00793	0.00192	0	0.00892	0.00119	0.00984
Rb	0.01423	0.00872	0.00892	0	0.00829	0.00914
Ti	0.00697	0.00167	0.00119	0.00829	0	0.01067
Zr	0.01032	0.01209	0.00984	0.00914	0.01067	0

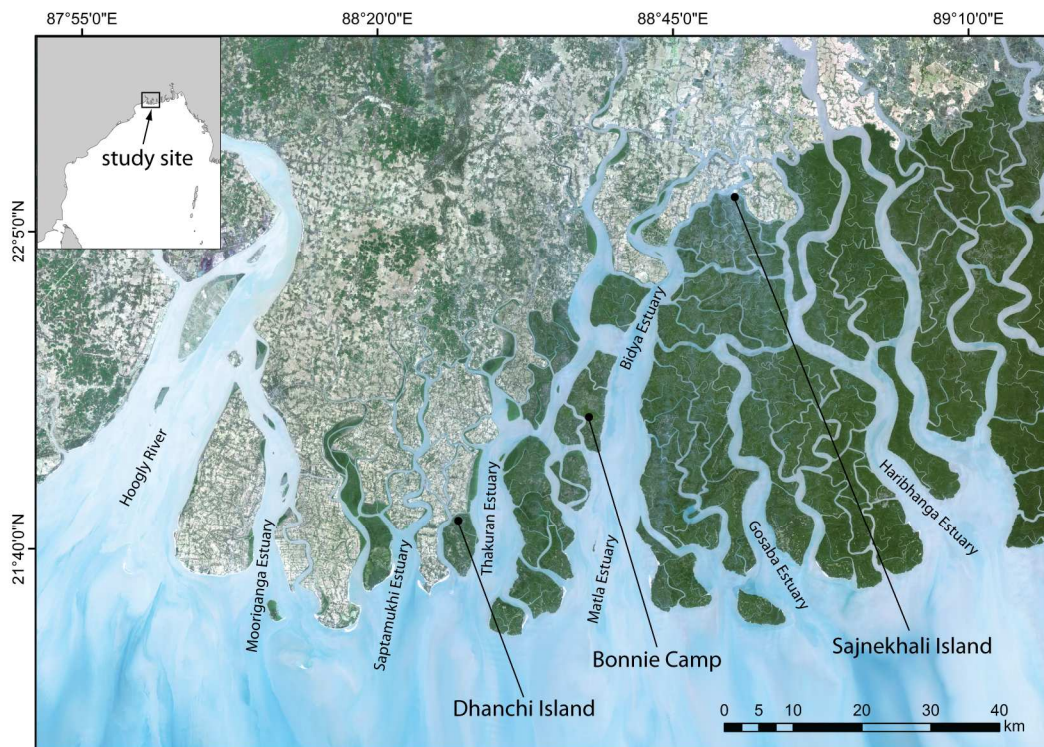
ACCEPTED MANUSCRIPT

	Ca	Fe	K	Rb	Ti	Zr
Ca	0	0.00951	0.00798	0.01435	0.00704	0.01044
Fe	0.00951	0	0.00194	0.00881	0.00168	0.01217
K	0.00798	0.00194	0	0.00909	0.0012	0.00987
Rb	0.01435	0.00881	0.00909	0	0.00833	0.0092
Ti	0.00704	0.00168	0.0012	0.00833	0	0.01068
Zr	0.01044	0.01217	0.00987	0.0092	0.01068	0

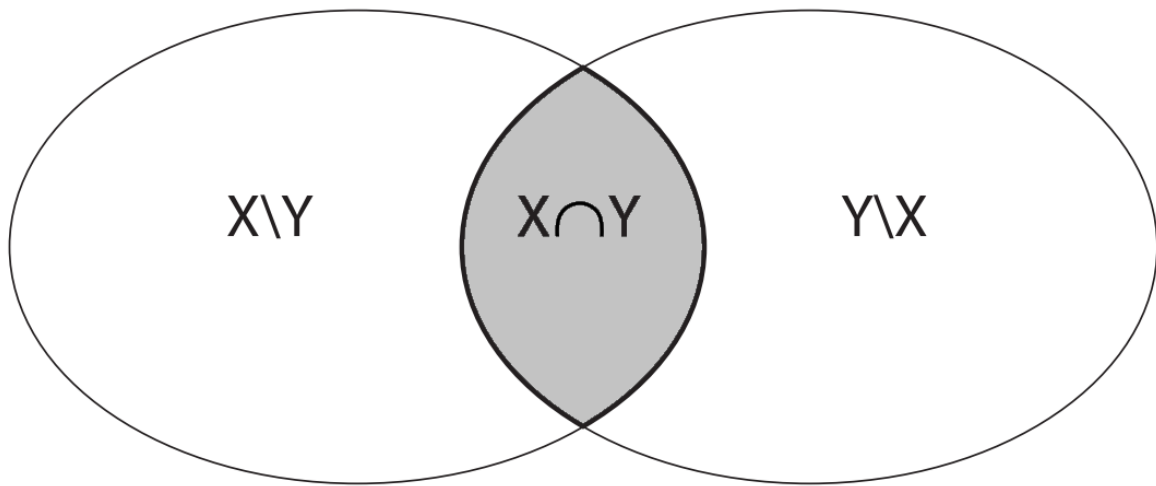
ACCEPTED MANUSCRIPT

	Ca	Fe	K	Rb	Ti	Zr	
Ca		0	0.9399	0.9602	0.9122	0.9593	0.9104
Fe	0.9399		0	0.5076	0.2524	0.4248	0.6758
K	0.9602	0.5076		0	0.3844	0.0773	0.7085
Rb	0.9122	0.2524	0.3844		0	0.4952	0.7768
Ti	0.9593	0.4248	0.0773	0.4952		0	0.6912
Zr	0.9104	0.6758	0.7085	0.7768	0.6912		0

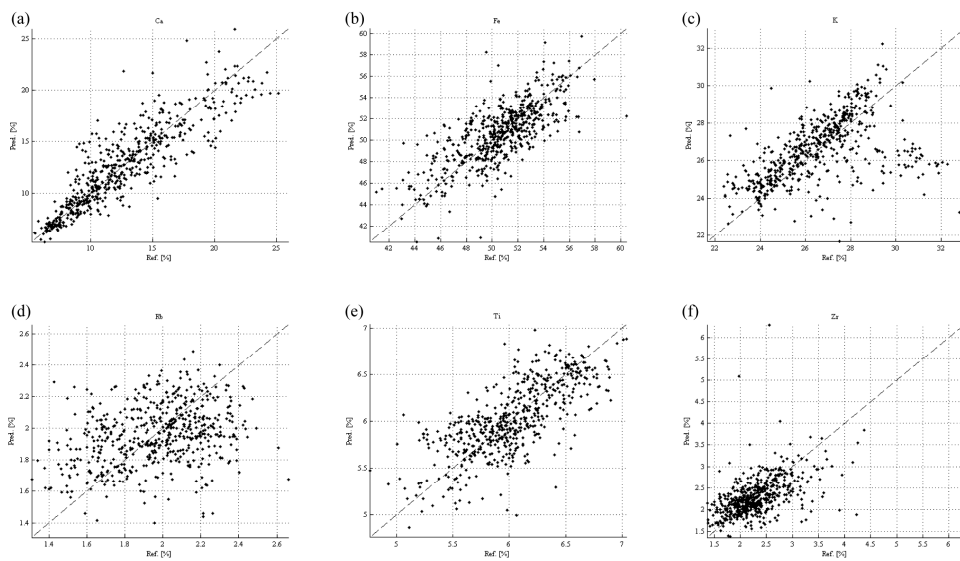




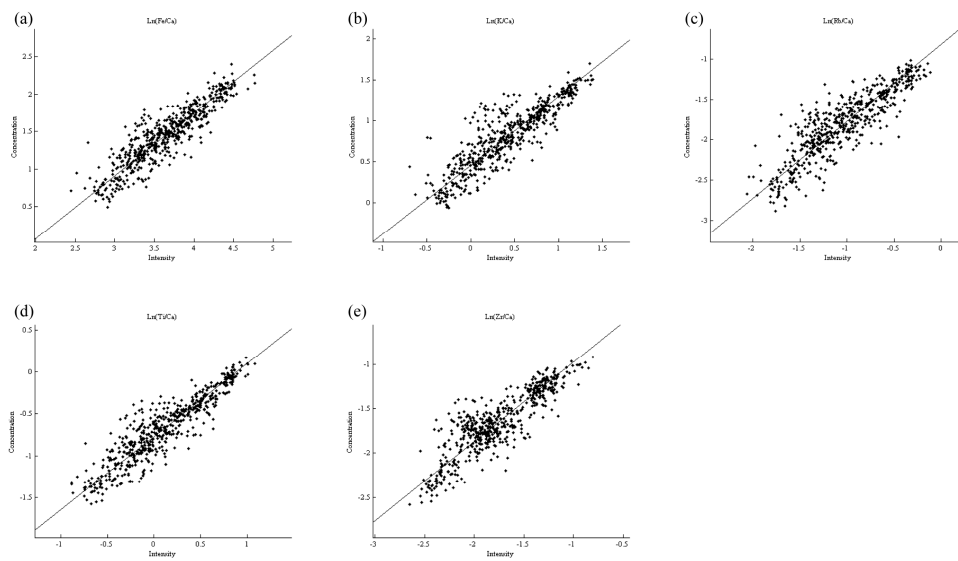
ACCEPTED MA



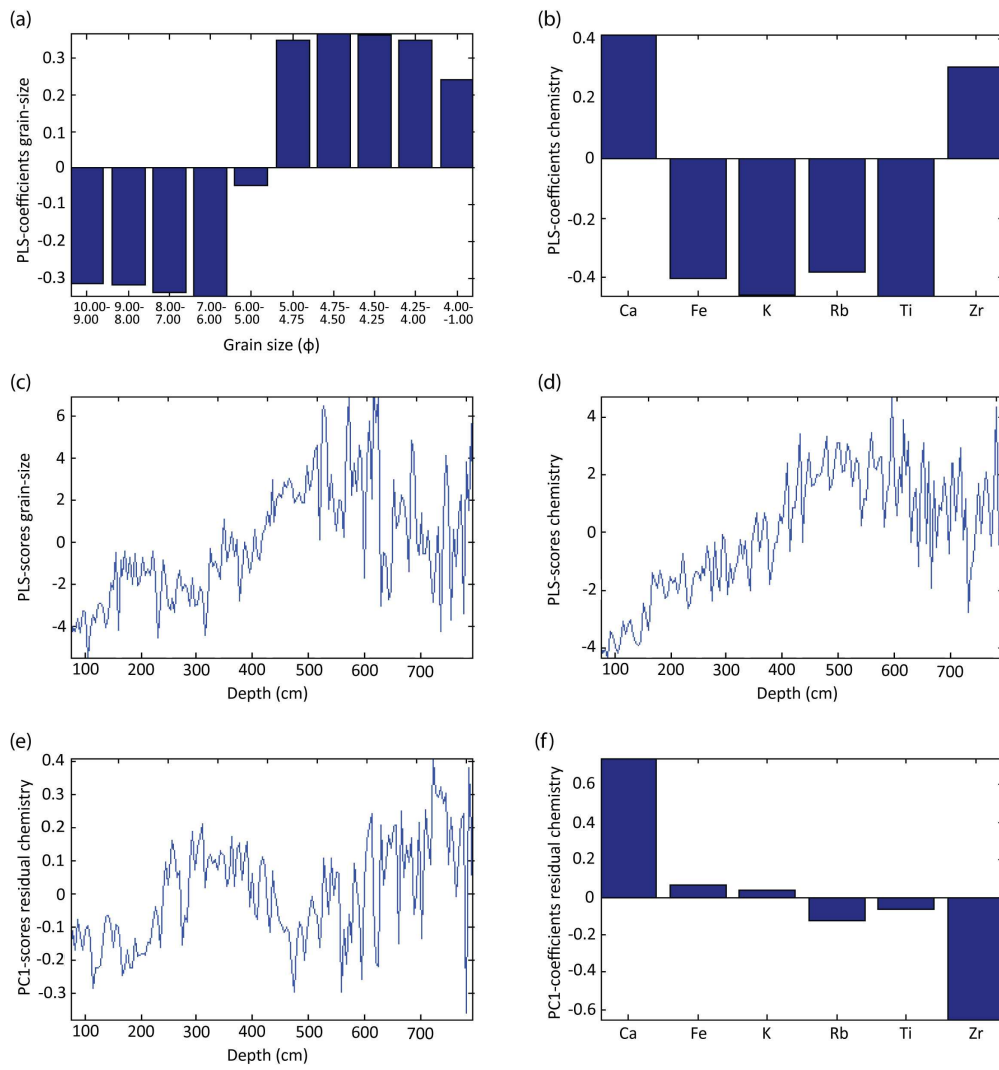
ACCEPTED MANUSCRIPT



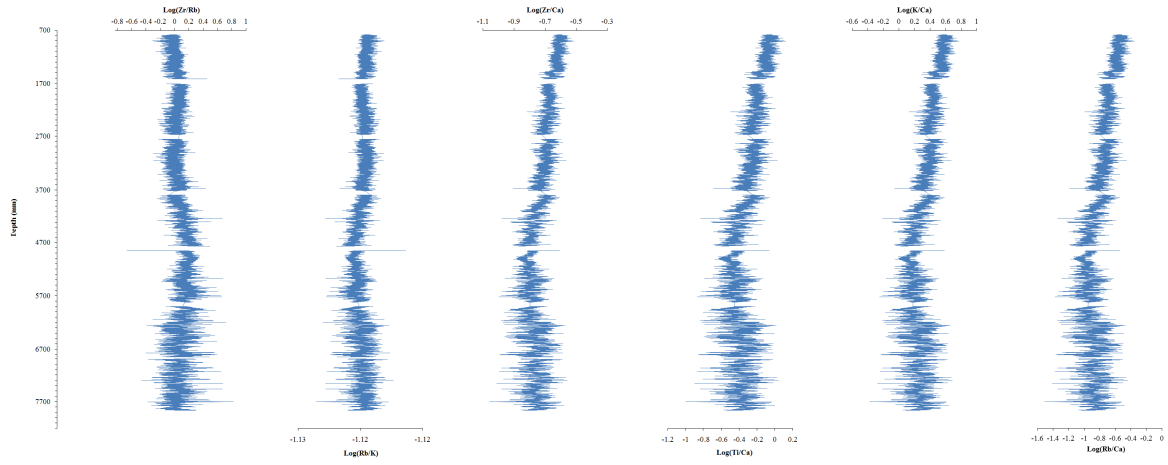
ACCEPTED MANUSCRIPT



ACCEPTED MANUSCRIPT



ACCEPTED



Highlights

- Multivariate statistical modelling of grain-size and geochemistry from the Holocene Ganges-Brahmaputra delta
- Compositional data analysis through log-ratio calibration and partial least squares modelling approaches for proxy depositional information
- Methodological framework for unravelling Holocene sedimentation patterns in the Ganges-Brahmaputra delta